PAPER • OPEN ACCESS

Dynamics of the pedestal transport during edge localized mode cycles at ASDEX Upgrade

View the article online for updates and enhancements.

Dynamics of the pedestal transport during edge localized mode cycles at ASDEX Upgrade

E Viezzer[1] , M Cavedon[2], P Cano-Megias[3] , E Fable[2], E Wolfrum[2],
D J Cruz-Zabala[1] , P David[2], R Dux[2], R Fischer[2], G F Harrer[4] ,
F M Laggner[5], R M McDermott[2] , U Plank[2], T Pütterich[2] ,
M Willensdorfer[2] and the ASDEX Upgrade Team

[1] Dept. of Atomic, Molecular and Nuclear Physics, University of Seville, Avda. Reina Mercedes, 41012 Seville, Spain
[2] Max Planck Institute for Plasma Physics, Boltzmannstr. 2, 85748 Garching, Germany
[3] Dept. of Energy Engineering, University of Seville, Camino de los Descubrimientos, 41092 Seville, Spain
[4] Institute of Applied Physics, TU Wien, Fusion@ÖAW, Vienna, Austria
[5] Princeton Plasma Physics Laboratory, Princeton, United States of America

E-mail: eviezzer@us.es

Abstract

The dynamic behaviour of the ion and electron energy, particle and momentum transport measured during type-I edge localized mode (ELM) cycles at ASDEX Upgrade is presented. Fast measurements of the ion and electron temperature profiles revelead that the ion and electron energy transport recover on different timescales, with the electrons recovering on a slower timescale (Cavedon *et al* 2017 *Plasma Phys. Control. Fusion* **59** 105007). The dominant mechanism for the additional energy transport in the electron channel that could cause the delay in the electron temperature gradient (∇T_e) recovery is attributed to the depletion of energy caused by the ELM. The local sources and sinks for the electron channel in the steep gradient region are much smaller compared to the energy flux arriving from the pedestal top, indicating that the core plasma may dictate the local dynamics of the ∇T_e recovery during the ELM cycle. A model for the edge momentum transport based on toroidal torque balance that takes into account the existence of poloidal impurity asymmetries has been developed. The analysis of the profile evolution during the ELM cycle shows that the model captures the dynamics of the rotation both before the ELM crash and during the recovery phase.

Keywords: magnetic confinement fusion, plasma transport, magnetohydrodynamics

(Some figures may appear in colour only in the online journal)

1. Introduction

Edge localized modes (ELMs) [1–3] are inherent to high-confinement mode (H-mode) plasmas, which are characterized by an edge transport barrier. This region of reduced particle and energy transport leads to steeper gradients in the temperature, density and pressure and a characteristic pedestal structure forms that typically extends over the outermost ~5% of the plasma. The pedestal primarily determines the increase in confinement and global stored energy compared to the low-confinement mode (L-mode) and is often regarded as boundary condition for the core plasma.

The pedestal can grow until a magnetohydrodynamic (MHD) limit is achieved. For type-I ELMs [1], this limit is thought to be determined by coupled peeling-ballooning

modes [4], which are driven by large edge current densities and steep pressure gradients. ELMs cause detrimental heat and particle fluxes which pose a threat for the lifetime of the plasma facing components and lead to a quasi-periodic degradation of the pedestal.

The destabilization of peeling-ballooning modes is the leading model to explain type-I ELMs [4, 5], however, the entire picture is not always captured by this model as some experiments have shown that additional physics may be needed to describe the triggering of ELMs [6–8]. Besides the global peeling-ballooning mode that has an effect on the entire pedestal structure, the presence of local modes can affect the plasma edge in a very narrow region [9, 10], causing transport and leading to a change of the pedestal structure locally [11–13]. Peeling-ballooning theory, combined with the assumption that kinetic ballooning modes [14, 15] set the pedestal width, describes the top of the pedestal in a variety of plasmas with different parameters [16]. However, the exact physics mechanism that determines the pedestal structure and transport is not yet clear.

For the ions, recent experiments provided evidence that the background $E \times B$ velocity profile, the ion heat transport and the impurity particle transport is determined by neoclassical processes [17–20]. For the electrons the mechanisms responsible for the electron heat and particle transport are multifold as they are dominated by turbulence [21–23]. Rotation has an important effect on regulating turbulent transport [24]. In the edge transport barrier, the shear in the $\mathbf{E} \times \mathbf{B}$ velocity is thought to be responsible for the turbulence suppression via decorrelation of the turbulent eddies [25, 26]. While the ion energy transport is close to the neoclassical level, residual ion transport that affects only the momentum channel could still be present, since, to lowest order, the momentum diffusivity in neoclassical theory is 0 [27]. Introducing effects that break the axisymmetry lead to a finite momentum diffusivity [28, 29], however, well below the neoclassical ion heat diffusivity, i.e. $\chi_\phi^{neo} \ll \chi_i^{neo}$.

Understanding the physics behind ELMs and the effect they cause on particle, energy and momentum transport is important for a predictive capability of future fusion devices as the anticipated transient heat and particle fluxes associated with unmitigated ELMs are expected to severely limit the lifetime of plasma facing components. In addition, comparison between experimental and theoretical heat fluxes allows us to further pin down the physics mechanism responsible for an ELM crash.

This paper extends our previous work [30–32] to the combined analysis of the ion and electron heat transport, as well as the behaviour of the momentum transport during the ELM cycle. Section 2 gives a brief review on the observations of the profile evolution during the ELM cycle. The energy transport simulations are introduced and discussed in section 3, while section 4 presents the modeling of momentum transport. Section 5 gives a summary and discusses the main results.

2. Experimental observations of inter-ELM profile evolution

Due to the small spatial width of the pedestal and the fast temporal changes associated to ELMs, high-resolution measurements are required for the analysis of the pedestal transport. Advances in the diagnostic capabilities on various tokamaks enabled access to the dynamics of the pedestal during the ELM cycle [7, 30, 33–40]. While the electron temperature and density are routinely available with a temporal resolution down to several tens of μs, measurements of the ion temperature on such a timescale are more challenging. The upgrade of the edge charge exchange recombination spectroscopy (CXRS) diagnostic at ASDEX Upgrade [41] enabled fast measurements of the impurity temperature, density and rotation profiles with a temporal resolution down to 50 μs. For typical conditions at ASDEX Upgrade, due to the thermal equilibration of ions and impurities, the measured impurity temperature represents a measurement of the ion temperature [32, 42].

Combining the sub-ms ion and electron measurements enables a detailed study of the recovery times in particle, energy and momentum transport. The electron and ion kinetic profiles collapse on a very fast time scale (tens to hundreds of μs) after the onset of a type-I ELM and show different time scales in the recovery phase [30, 37, 40, 43]. Comparing the ion to the electron temperature profile revealed that the maximum ion temperature gradient, ∇T_i, reaches its pre-ELM value after the ELM crash on a faster timescale than the maximum electron temperature gradient, ∇T_e, [30]. The ion temperature and electron density gradient recover to their pre-ELM values on similar timescales (3–4 ms), while the ∇T_e recovers on a slower timescale and reaches the pre-ELM values only 7–8 ms after the ELM onset (see also figure 1). The reader is also referred to figure 5 of [30] for a comparison of the radial profiles before, during and after the ELM. The saturation of ∇T_i and ∇n_e is correlated with the onset of medium-frequency fluctuations ($f \approx 50$ kHz) [44], while high-frequency fluctuations ($f \approx 250$ kHz) appear when ∇T_e recovers [40], indicating a different clamping mechanism for the ion energy and electron energy and particle transport. Similar observations were made at DIII-D [34, 39, 45].

3. Simulations of the energy transport

The dynamic behaviour of the pedestal transport during an ELM cycle at AUG is studied by combining a comprehensive set of pedestal measurements with modeling. The simulations are based on the transport code ASTRA [46] coupled with the free-boundary equilibrium code SPIDER [47]. For the simulations presented here, the equilibrium geometry of the separatrix is given as input and the fixed-boundary high-resolution equilibrium solver module of SPIDER is used.

ASTRA solves the time dependent and flux surface averaged energy transport equation using the measured electron temperature and density, ion temperature and radiated
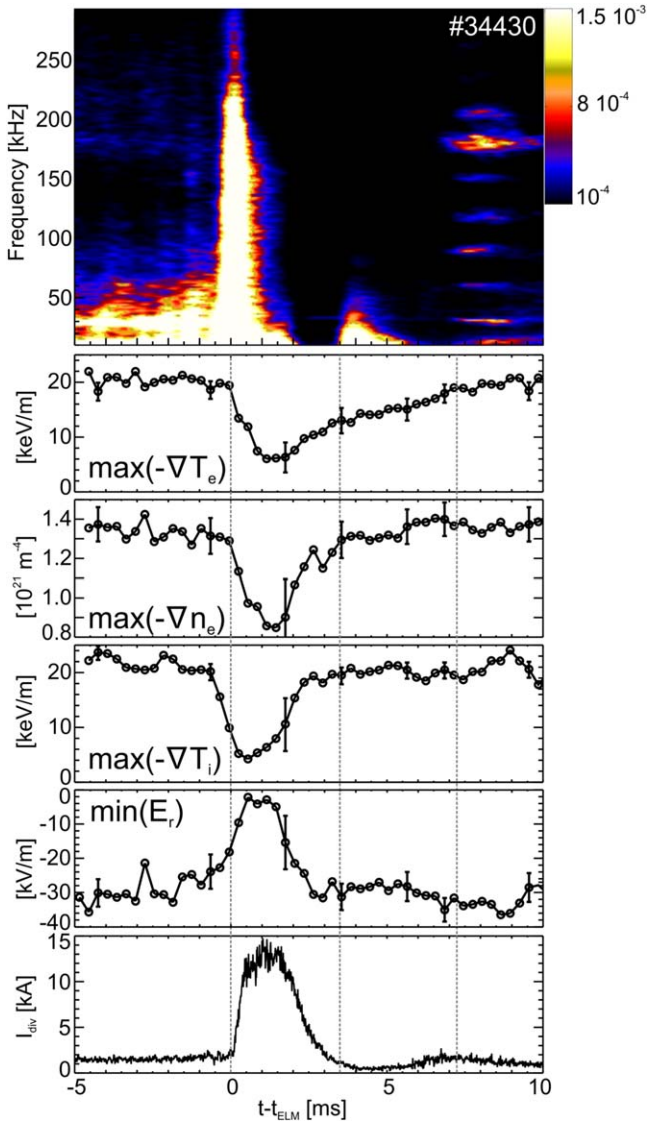
Figure 1. ELM-resolved frequency spectrogram measured with a magnetic pick-up coil (a), maximum electron temperature gradient (b), density gradient (c), ion temperature gradient (d) and minimum in the E_r well (e) during the ELM cycle. The onset of the ELM is indicated by a measurement of the divertor shunt current (f). Here, the ion and electron measurements (100 μs time resolution) were binned to a temporal resolution of 300 μs to take into account possible mis-synchronizations of single frames. Reproduced from [32]. CC BY-NC-ND 4.0.

Figure 2. (a) Pre-ELM ion and electron heat diffusivity (black and blue) compared to the neoclassical prediction (red for ions, magenta for electrons) using the NEOART code. The dashed gray lines indicate the region for the measured E_r profile in (b).

power profile as input. The energy sources are calculated from the auxiliary input heating power (here, neutral beam injection, $P_{e,NBI}$ and $P_{i,NBI}$, and electron cyclotron resonance heating, $P_{e,ECRH}$), the electron-ion heat exchange rate, P_{ei}, losses due to atomic processes (P_e^N and P_i^N) such as charge exchange, ionization and recombination; for the electrons, losses due to radiation, P_{rad}, and the ohmic power, P_{oh}, are also contributing in the power balance:

$$P_e = P_{e,NBI} + P_{e,ECRH} + P_{oh} - P_{rad} - P_{ei} - P_e^N, \quad (1)$$

$$P_i = P_{i,NBI} + P_{ei} + P_i^N. \quad (2)$$

The heat flux is determined by the volume integration of the energy sources and sinks and relates the temperature gradient
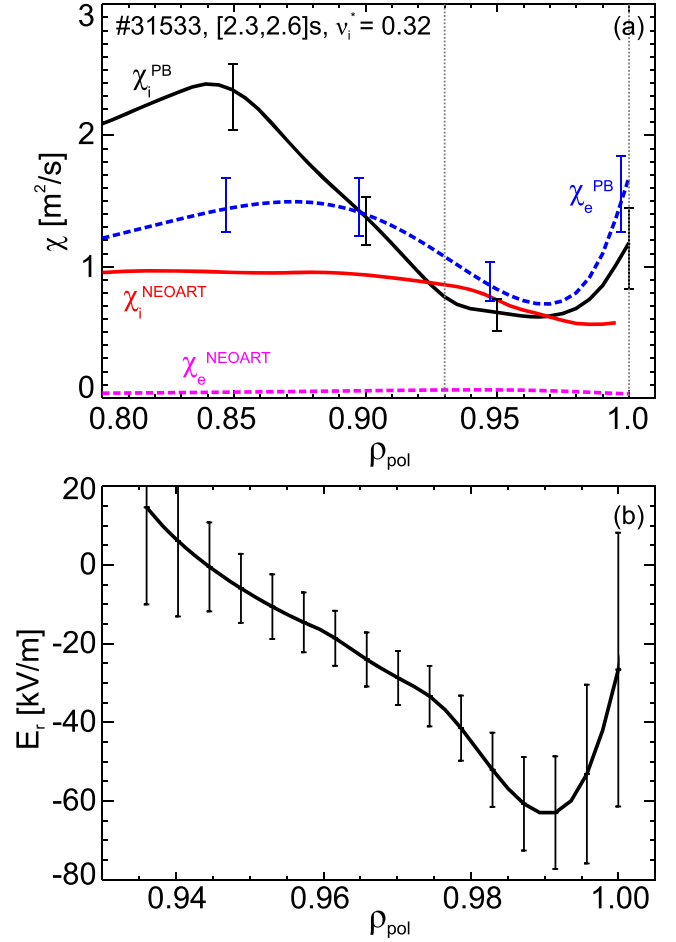
to the heat diffusivity:

$$Q \propto -\chi n \frac{\partial T}{\partial \rho} \frac{\partial V}{\partial \rho} \langle (\nabla \rho)^2 \rangle. \quad (3)$$

Figure 2 shows the pre-ELM profile of the ion (black) and electron (blue) heat diffusivity as determined from power balance analysis for a low collisionality discharge ($\nu_i^{*,ped} = 0.32$ at the pedestal top), where the ion and electron temperature are well separated. The neoclassical heat diffusivities as calculated with the NEOART code [48] are shown in red (ions) and magenta (electrons). The ion heat diffusivity is close to the neoclassical level in the steep gradient region, while further inwards the experimentally determined χ_i exceeds the neoclassical prediction by a factor of 2–3. Note that close to the separatrix, where the ordering of standard neoclassical theory starts to break down, the experimentally determined χ_i is also higher compared to the neoclassical one. The electron heat diffusivity is well above the neoclassical level, throughout the pedestal region, showing that the electron heat channel is dominated by anomalous transport.

The neoclassical ion heat diffusivity is observed in the maximum ∇T_i region, not across the whole pedestal. For the conditions in the pedestal of AUG, it typically covers 2–3
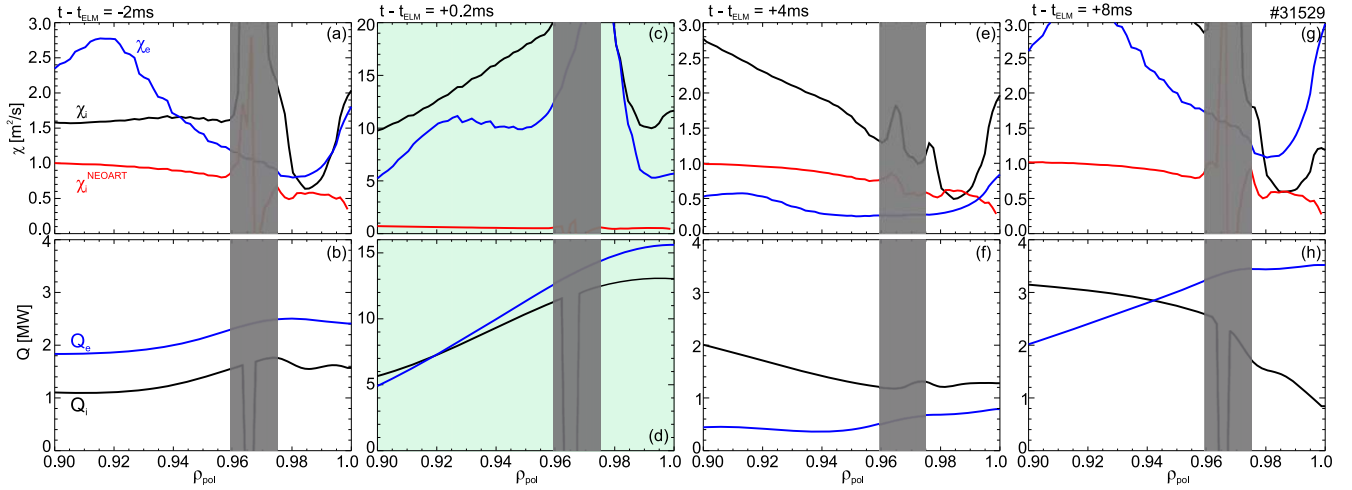
Figure 3. Heat diffusivities and heat fluxes for ions (black) and electrons (blue) at four time points during the ELM cycle. Note that (c) and (d) have a different scale in the *y*-axis.
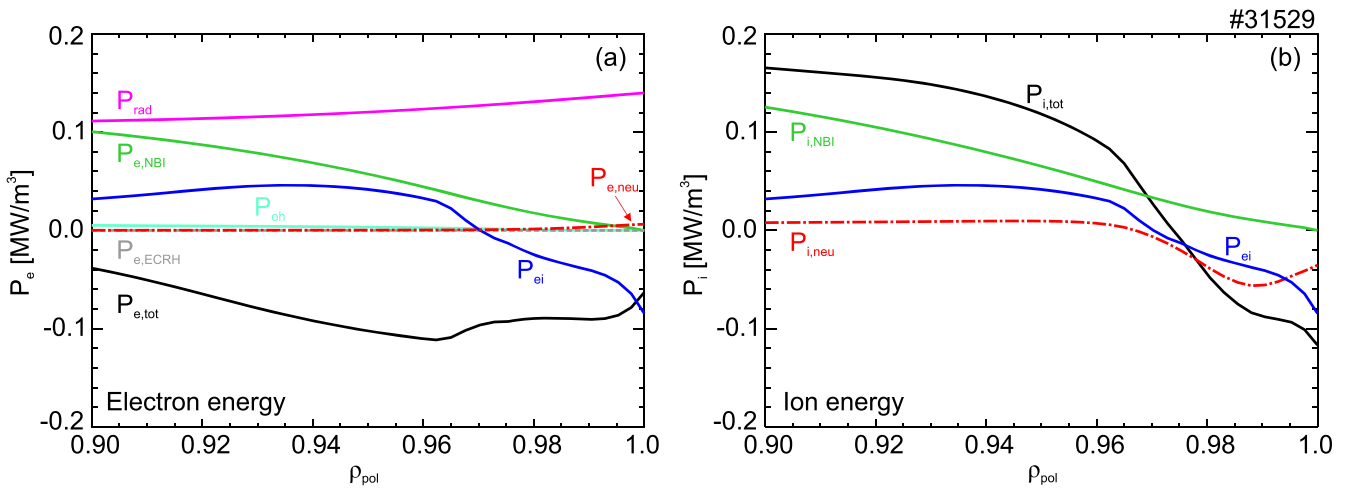

Figure 4. Pre-ELM electron (a) and ion (b) energy sources and sinks at the plasma edge. The total energy source is shown in black, while the electron-ion heat coupling term is shown in blue, the energy source due to NBI in green and due to ECRH in gray, the radiated power in magenta, the ohmic power in turquoise and the term associated to atomic processes in red.

poloidal ion gyroradii. Comparison to the E_r profile shows that the radial extent of the region, where the ion heat diffusivity is close to the neoclassical level, is localized in the inner part of the E_r well (see figure 2(b)). This coincides with the radial location of the maximum $E \times B$ shearing rate and the maximum ion pressure gradient [42], further supporting that the inner E_r shear layer may be the important region for suppressing turbulent transport in the H-mode edge [49].

Figure 3 shows the radial profiles of the heat diffusivities (upper panel) and heat fluxes (lower panel) for four different time points during the ELM cycle. Note that the heat diffusivities and fluxes were determined using time-dependent power balance analysis taking into account the temporal variation in the plasma energy. Figures 3(a), (b) show the pre-ELM profiles (-2 ms), (c), (d) the profiles during the ELM ($+0.5$ ms), (e), (f) the post-ELM profiles when the maximum ion temperature and electron density gradients have recovered ($+4$ ms) and (g), (h) the post-ELM profiles when the maximum ∇T_e has recovered ($+8$ ms). Note the different scale in

the *y*-axis for (c), (d). For comparison, the neoclassical χ_i is shown in red. Good agreement with neoclassical theory is obtained in the steep gradient region before and after the ELM crash. The area highlighted in gray corresponds to the region where the slower edge (2.3 ms) and core CXRS measurements (5 ms) overlap with the fast edge CXRS system (65 μs). As the measurements of the slower systems are interpolated onto the fast temporal grid, unphysical gradients are introduced.

During the ELM cycle, the ion heat diffusivity recovers to the neoclassical level as soon as the maximum ion temperature gradient reaches its pre-ELM value [31]. Note that during this time period the electron heat flux is lower than the ion heat flux (see figure 3(f)), indicating that the electron heat flux is small. Later in the ELM cycle the electron heat channel has recovered back to its pre-ELM level (see figure 3(h)).

The distribution of the sources and sinks for the electron and ion energy is shown in figure 4. In the edge transport barrier, the radiated power and the heat exchange rate
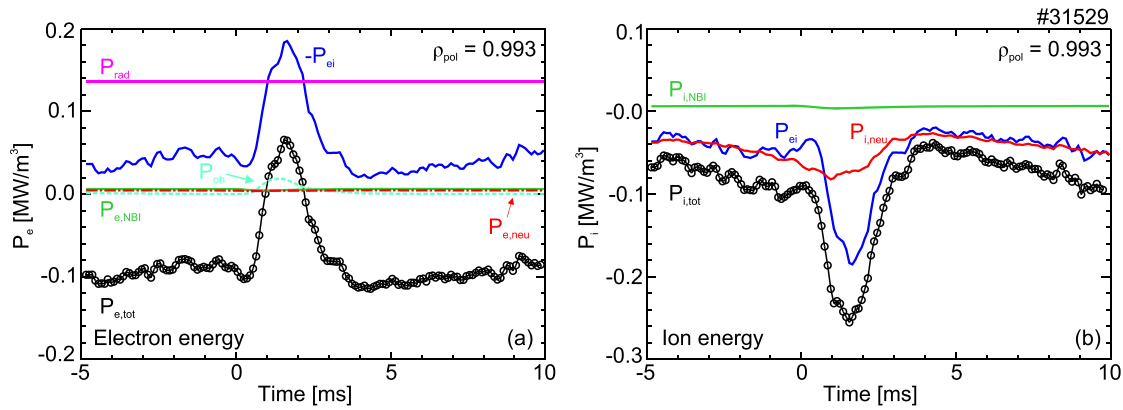
Figure 5. Temporal evolution of electron (a) and ion (b) energy sources during the ELM cycle. Note that in (a) $-P_{ei}$ is shown to indicate that this term is an energy source for the electrons.

between electrons and ions are dominant for the electrons, while for the ions both the electron-ion coupling and atomic processes play an important role. P_{ei} is negative in the pedestal region, i.e. power is going from the ions to the electrons. Note that ASTRA models the neutrals with an effective input source Γ_N. As the neutral distribution cannot be directly measured we have scanned the neutral influx between 10^{20} and $10^{22}\,\mathrm{s}^{-1}$. Increasing the neutral influx in the transport simulations shows a small effect on the electron power balance, indicating that atomic processes play a minor role for the delay of the ∇T_e recovery [32]. The profiles shown in figure 4 correspond to $\Gamma_N = 3.3 \times 10^{21}\,\mathrm{s}^{-1}$.

Figure 5 shows the evolution of the energy sources and sinks during the ELM cycle. Note that we assumed the power losses due to radiation to be constant during the ELM cycle as the deconvolution of the bolometry measurements during the ELM crash has too large uncertainties. The coupling between ions and electrons plays an important role. As the separatrix ion temperature increases during the ELM crash, the difference between T_i and T_e in the steep gradient region gets larger leading to an increase in P_{ei}. As P_{ei} is subtracted in the electron energy balance, the total electron energy source is close to 0 during the ELM crash, while for the ions it is added and gives a total net increase. Figures 4 and 5 also show that the local ion and electron energies are small at the plasma edge, indicating that the changes of the local sources and sinks are too small to explain the delay in the ∇T_e recovery.

A comparison to the divergence of the heat flux, i.e. the heat flux rate that exits the plasma, shows that shortly after the ELM onset, the electron energy flux arriving from the plasma core is much larger compared to the local P_e (see figure 6). In figure 6(a) the electron temperature, (b) the electron heat flux rate, the local P_e (dashed line) and (c) the electron heat diffusivity are shown at 3 different radial positions, inside the pedestal top and in the steep gradient region ($\rho_{pol} = 0.95$, 0.98 and 0.99). The electron temperature at the pedestal top already starts to recover while the ELM is still active (as shown in the divertor shunt current measurements in figure 1(f)). Shortly after the ELM, the divergence of the electron heat flux shows a maximum inside the pedestal top (area highlighted in blue in figure 6), while the changes in the
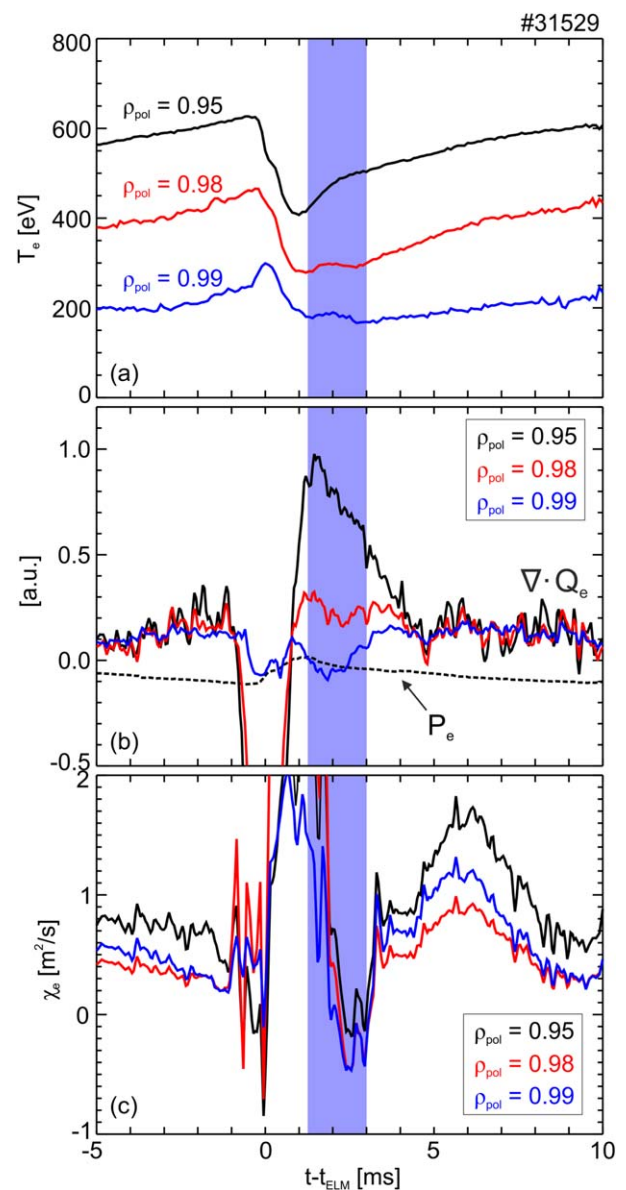

Figure 6. Temporal evolution of the electron temperature, electron heat flux rate, the local electron energy and the electron heat diffusivity during the ELM cycle at three different radial positions. For clarity, only the local P_e at $\rho_{pol} = 0.95$ is shown in (b).
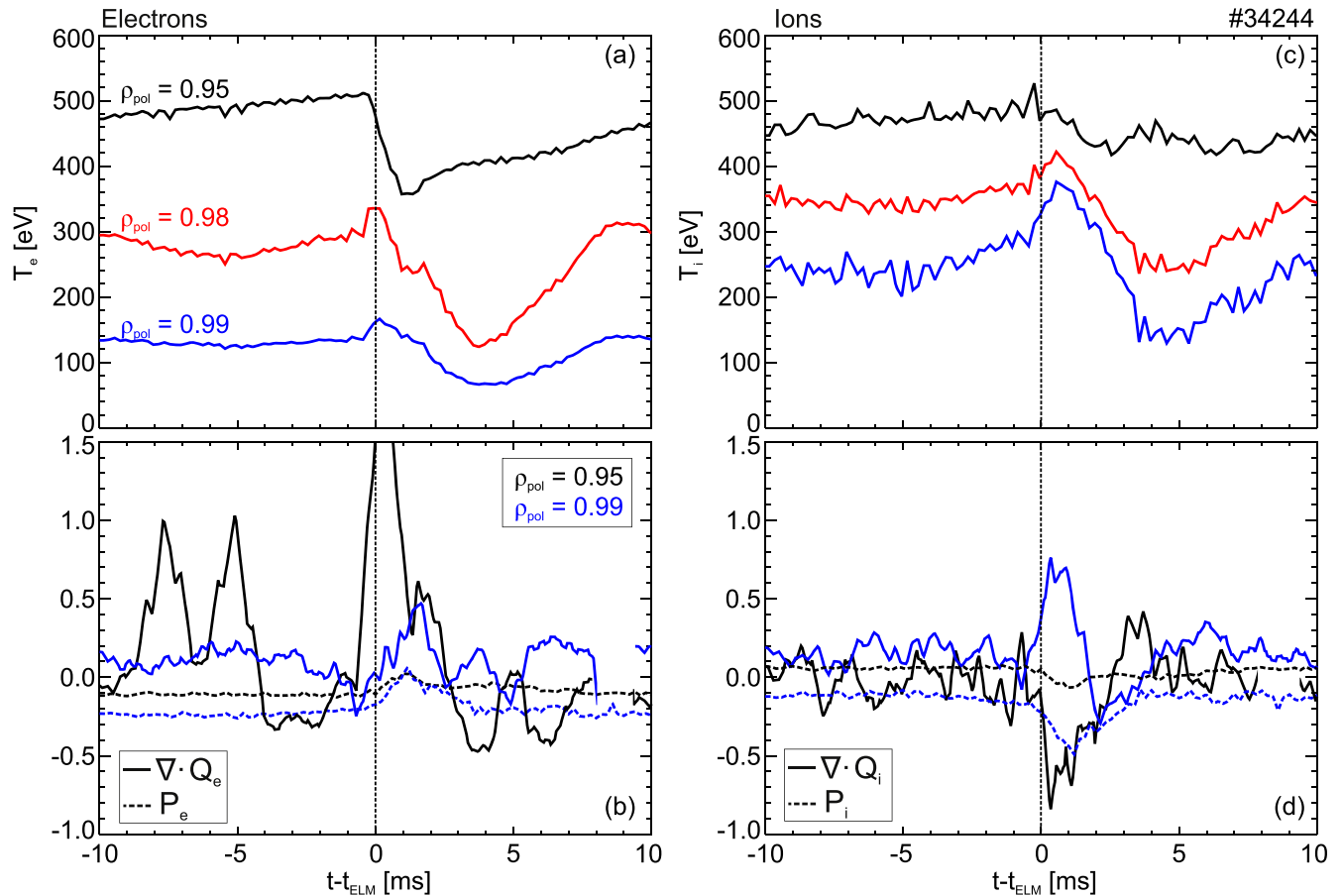
Figure 7. Temporal evolution of the electron and ion temperature, electron and ion heat flux rate in comparison with the local energy during the ELM cycle at three different radial positions. For clarity, only the pedestal top ($\rho_{pol} = 0.95$) and bottom $\rho_{pol} = 0.99$) are shown in figures (b) and (d).

local P_e remain small. At the same time, the electron heat diffusivity is close to 0, i.e. the electron heat transport is at a very small level. This indicates that the electron heat flux from the core plasma dominates the local dynamics, i.e. the heat flux is first recovered inside the pedestal top and needs a certain time to propagate through the pedestal, thus leading to a delay in the ∇T_e recovery.

To further test this hypothesis and compare the behaviour to the ion channel, we have applied the same analysis to a discharge in which ion temperature measurements are available for a larger radial region, covering $\rho_{pol} = 0.95$–1.0. The data from a type-I ELMy period (2.5–5.5 s) of an H-mode discharge ($B_t = 2.5$T, $I_p = 0.8$ MA, core line-averaged electron density of 6×10^{19} m^{-3}, NBI heating of 2.5 MW, ECRH of 1.2 MW and an ELM frequency of 45 Hz) has been synchronized with respect to the ELM onset. In this case, the time resolution for the ion measurements was restricted to the standard edge CXRS system with a time resolution of 2.3 ms. A smearing effect is introduced as the data is taken during a framing period of 2.3 ms, however, the global evolution is still visible. A similar behaviour is observed, first the ion temperature and electron density gradient recover, followed by a recovery of the ∇T_e (see figure 7). Also here, we observe that the electron heat flux rate from further in is much larger compared to the local electron energy source. For the ions,

this effect is much smaller (see figure 7(d)). The pedestal top of the ion temperature shows a very small effect due to the ELM crash. Note also that compared to the electrons, the ion heat transport cannot reach very small levels of $\chi_i \approx 0$, since the minimum ion heat diffusivity is given by neoclassical theory.

The transport analysis presented above indicates that the delay in the recovery of the ∇T_e is related to the depletion of the ELM in the edge region of the plasma. The electron energy flux arriving from inside the pedestal top dominates over the local energy sources, suggesting that first the pedestal top is recovered and then the steep gradient region of T_e. For the ions, this effect is small as the minimum χ_i is given by $\chi_i \approx \chi_i^{neo}$ and the ion heat flux is re-established again to its pre-ELM level shortly after the ELM crash.

4. Momentum transport modeling

Plasma rotation has a beneficial effect on plasma confinement as it reduces anomalous transport by flow shear stabilization [25, 26, 48]. It also affects the MHD stability of peeling-ballooning modes [50–52] and could therefore play an important role in ELM physics. Due to the symmetry of a tokamak, the toroidal rotation is not damped and is basically a
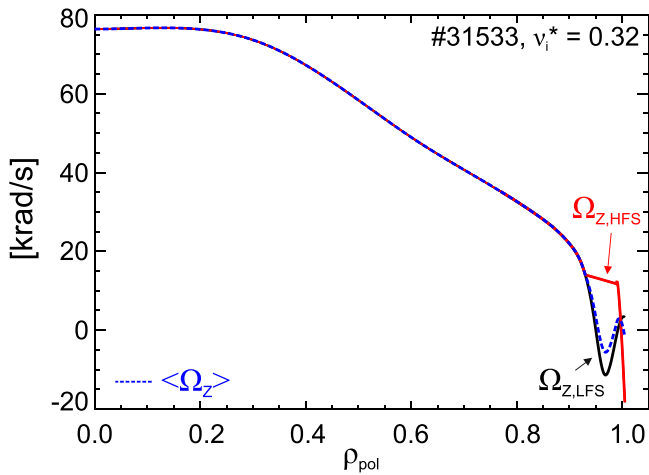
Figure 8. Toroidal angular rotation profile at the low-field side (LFS), high-field side (HFS) and the flux surface averaged profile taking into account the presence of the poloidally asymmetric flow structure.

Figure 9. Comparison of experimentally determined and simulated flux surface averaged profile for impurities and main ions.

free parameter. Previous studies on momentum transport show that the momentum and ion heat transport are strongly interlinked [53–56] with the momentum and ion heat diffusivity assuming similar values in plasmas with dominant neutral beam heating. In contrast, in discharges with no direct momentum input an intrinsic rotation level was observed and has opened an active field of research [57–62].

The evolution of the toroidal rotation is determined by the angular momentum balance equation:

$$mn\left\langle R^2\frac{\partial\Omega}{\partial t}\right\rangle = \langle RT_\phi\rangle - \langle R\vec{e}_\phi\nabla\cdot\mathbf{\Pi}_\phi\rangle, \qquad (4)$$

where m is the species mass, n the density, R the major radius, Ω the angular rotation frequency, T_ϕ the various torques that act on the plasma, $\vec{e}_\phi$ the unit vector in toroidal direction and $\mathbf{\Pi}_\phi$ the anisotropic stress tensor in toroidal direction. $\langle\cdot\rangle$ denotes the flux surface average. External torques that act on the plasma are e.g. neutral beam injection or friction with thermal neutrals [63]. For the modeling presented here, an effective diffusivity, i.e. diffusion, pinch, residual stress, and external momentum sources (NBI and neutral friction), is considered in ASTRA [46, 64]. Neutrals [63] can act as source via recycling and are taken into account in ASTRA using an effective neutral influx. A scan in the effective flux was performed and shows that the impact of neutrals is small. Note that the source profile plays an important role for the particle transport [22, 65, 66]. For the simulations presented here, the experimental density was used as input.

As the momentum acts on the flux surface average, we have developed a workflow that takes into account the existence of poloidal impurity asymmetries [67–70]. In-out asymmetries were observed in the impurity flow structure which can be explained by an excess of impurity density at the inboard side of the tokamak. A fluid model including the centrifugal forces due to inertia, the electric force, the pressure drive and the friction force was developed to study the nature of the parallel impurity dynamics [71]. It shows that the impurity asymmetry arises due to an interplay of all terms,
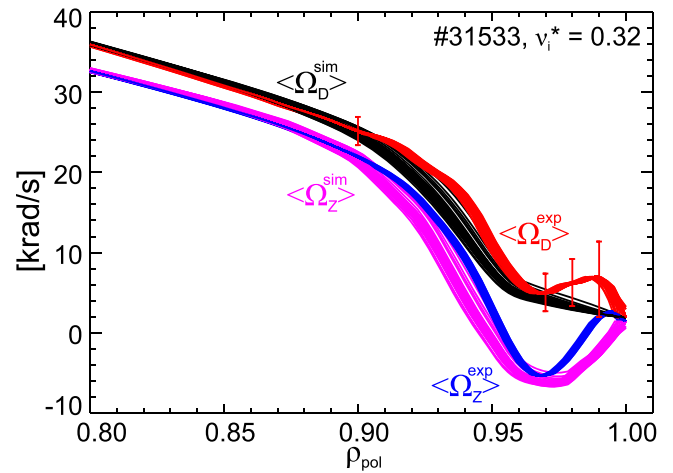
with the poloidal centrifugal force and the friction force playing a dominant role in the pedestal [71]. The model quantitatively reproduces the flow measurements and predicts the flow structure along the whole flux surface. As the HFS diagnostic [42, 72] is not a standard diagnostic that measures in every discharge we have used the fluid model to calculate the flux surface averaged flow profile. Figure 8 shows a comparison of the angular rotation frequency at the LFS and the HFS, and the flux surface averaged profile in blue (dashed line). The profile at the plasma edge is slightly altered, however, notice that the minimum in the edge rotation profile is still visible.

The analysis was applied to the pre-ELM phase of the low collisionality discharge and then extended to the profile evolution during the ELM cycle, the same discharges as presented in section 3. For the modeling, the torque density and momentum diffusivity profiles calculated with TRANSP [73] are used as input. The momentum diffusivity calculated with TRANSP is used for the core profile, while for the pedestal region $\chi_\phi \approx \chi_i$ is applied. Note that the effective momentum diffusivity used represents diffusion and the source terms that drive intrinsic rotation. As the plasma is NBI-heated, diffusion is expected to be the dominant term. In addition, an ad hoc Coriolis pinch following [74] is included, i.e. $v_{CP} = -\left(a_1 + a_2\frac{R}{L_{ne}}\right)\frac{\chi_\phi}{R}$, where R/L_{ne} is the density gradient scale length, R the major radius and a_1 and a_2 the cofficients that, together with the core χ_ϕ, are adjusted such that the core profile matches the measured rotation profile. At the plasma edge, the Coriolis pinch is set to 0.

As the toroidal momentum balance is solved for the main ions, the impurity toroidal rotation profile is calculated from the modeled main ion toroidal rotation applying the neoclassical correction in order to compare it to the experimental profile. Figure 9 shows a comparison of the simulated and measured flux surface averaged toroidal rotation profile for both main ions and impurities at the plasma edge for the low collisionality discharge. The estimated uncertainties for the main ion toroidal angular rotation frequency have been
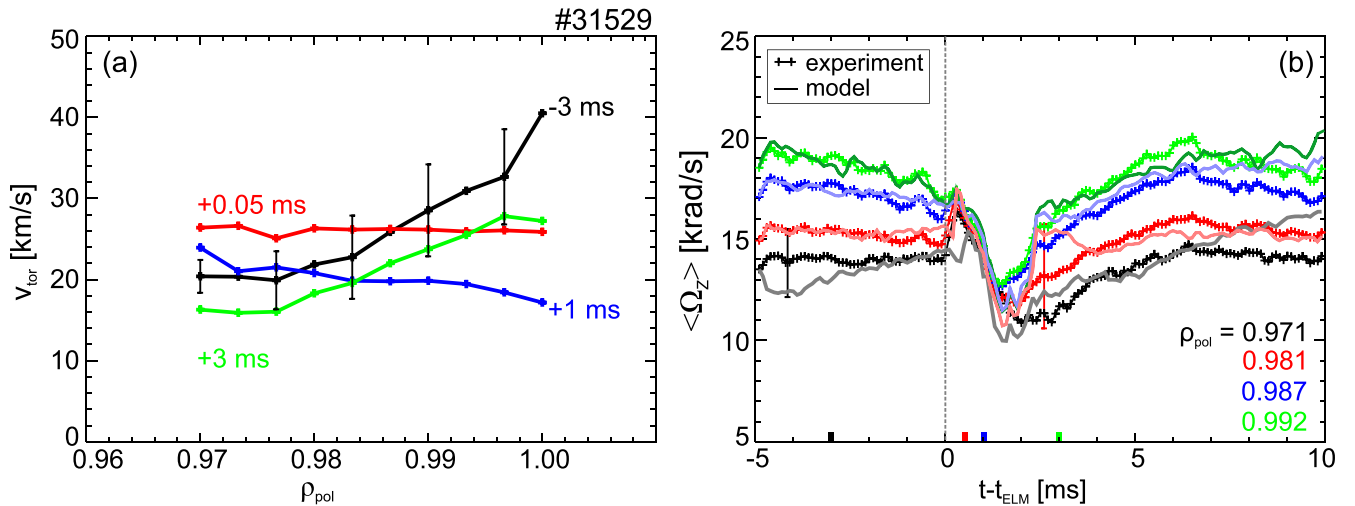
Figure 10. (a) Measured toroidal impurity rotation profile at four different time points during the ELM cycle, (b) temporal evolution of flux surface averaged toroidal impurity rotation at four radial positions. Comparison of experimental (crosses) and modeled (solid lines) flux surface averaged rotation profile. The time points shown in (a) are highlighted in (b) with the corresponding color coding. For clarity, the experimental uncertainties in (a) are only given for one time point.

estimated from the uncertainties on the measured impurity rotation profile and the uncertainties in the neoclassical correction. The modeled profile describes the experimental profile within the uncertainties.

The analysis was extended to the ELM-resolved measurements. Note that here the fast measurements are restricted to the pedestal region covering $\rho_{pol} = 0.97$–1.0, i.e. the outer shear layer of the dip in the toroidal impurity rotation. Figure 10 shows (a) the measured toroidal impurity rotation profile for four different time points with respect to the ELM onset, while (b) shows the temporal evolution at 4 radial positions during the ELM cycle. The experimental data is highlighted with crosses, while the simulation is shown with solid lines. Before the ELM crash, the toroidal rotation profile has a pronounced minimum close to the pedestal top ($\rho_{pol} = 0.97$), while towards the separatrix the rotation increases. During the ELM, the pedestal top rotation increases, while the separatrix rotation decreases leading to a flatter profile. The toroidal impurity rotation shows a similar behaviour as the T_i profile, the toroidal rotation flattens out and then the whole edge profile drops (see blue profile in figure 10(a)). The toroidal impurity rotation profile recovers to its pre-ELM profile on the same timescale as the recovery of the ion temperature gradient and radial electric field [30], and shows its pre-ELM dip 3–4 ms after the ELM onset.

For simplicity and since the dominant driving terms during the ELM are not known, we assumed a purely diffusive effect in order to simulate the ELM crash itself, i.e. we artificially increased the effective diffusion coefficient. Note that this is a very simplified assumption and disentangling the effects due to diffusion and pinch is subject to future work. In this work, we are interested in the recovery phase after the ELM and since the dynamics has an effect on later time points we simulated the impact of the ELM with an increase in the effective diffusivity to capture the toroidal impurity rotation during the ELM and to set the correct starting conditions for

the post-ELM recovery. Figure 10(b) shows the temporal evolution of the experimental (crosses) and modeled toroidal impurity rotation (solid lines) at four distinct radial positions ($\rho_{pol} = 0.97$–0.993). The model captures the behaviour of the toroidal rotation dynamics during the recovery phase, indicating that in dominant NBI heated discharges viscosity and external momentum input are the dominant terms in the toroidal momentum balance. As shown in figure 10(b), the small overshoot of the model at $\rho_{pol} \approx 0.98$ after the ELM crash is within the experimental uncertainties.

Combined with the observations on the ion and electron heat transport channels, the following picture emerges: the impurity rotation dynamics is dominated by the main ion pressure gradient via the neoclassical differential rotation. The rotation is observed to recover very quickly, on the same time scale as the ion temperature gradient [30], as expected. As the $E \times B$ rotation and its shear are dominated by the ion pressure gradient, the ion fluctuations are reduced rapidly, thus allowing the fast restoration of the H-mode after the ELM crash. This is consistent with the observation of a neoclassical ion heat flux and suggests that the mode that arises during the ELM mainly acts on the electrons. This is in line with the pedestal transport fingerprints identified in [21, 75] and points towards the electron temperature gradient (ETG) or microtearing (MTM) nature of this mode.

5. Summary and conclusions

Modeling of the transport channels allows us to shed light on the dynamic behaviour of the transport coefficients during the ELM cycle. For the experimental range studied on ASDEX Upgrade the ion heat transport was observed to be close to the neoclassical level before the ELM crash in the region where the edge ion temperature gradient is maximal, while further inwards the ion heat transport is about a factor of 4–5 above

the neoclassical level [31]. The region where the ion heat transport is close to neoclassics coincides with the inner part of the E_r well, further supporting that the inner E_r shear layer may be the important layer for turbulence reduction. The analysis of the edge transport also suggests that the mode that is present in the steep gradient region predominantly acts on the electrons, since the ion heat transport is observed to be neoclassical.

Possible mechanisms for the additional energy transport in the electron channel that could cause the delay in the ∇T_e recovery, were studied. The local sources and sinks for the electron channel in the steep gradient region are much smaller compared to the electron energy flux arriving from the plasma core shortly after the ELM crash. At the same time a very small electron heat transport level ($\chi_e \approx 0$) is observed. This indicates that after the ELM crash, first the pedestal top is re-established as the energy flux from the plasma core arrives. Since the heat pulse needs a certain time to propagate through the pedestal, this could cause the observed delay in the recovery of the ∇T_e. For the ions, this effect is small as χ_i has a lower limit that is determined by neoclassics.

The toroidal momentum transport has been studied using toroidal torque balance analysis based on viscosity, pinch and external and internal momentum sources. The model has been extended to include the presence of poloidal impurity asymmetries. At the plasma edge, the toroidal momentum is modeled using an effective diffusivity. The ELM itself has been simulated artificially by increasing the momentum diffusivity to recover the behaviour of the rotation during the ELM crash and to match the starting conditions for the profile recovery. Comparison of the experimental and simulated flux surface averaged rotation shows that the dynamics of the edge momentum transport is reproduced by the model both before the ELM crash and during the recovery phase. This indicates that external momentum sources and viscosity are the main players in dominant NBI-heated discharges.

Acknowledgments

ORCID iDs

E Viezzer ● https://orcid.org/0000-0001-6419-6848
P Cano-Megias ● https://orcid.org/0000-0001-5182-6513
D J Cruz-Zabala ● https://orcid.org/0000-0001-5925-5153
G F Harrer ● https://orcid.org/0000-0002-1150-3987
F M Laggner ● https://orcid.org/0000-0003-1601-2973
R M McDermott ● https://orcid.org/0000-0002-8958-8714
T Pütterich ● https://orcid.org/0000-0002-8487-4973
M Willensdorfer ● https://orcid.org/0000-0002-1080-4200

References

[1] Zohm H 1996 *Plasma Phys. Control. Fusion* **38** 105
[2] Loarte A *et al* 2006 *Nat. Phys.* **2** 369
[3] Wilson H *et al* 2008 *Fus. Sci. Technol.* **53** 161
[4] Snyder P B *et al* 2002 *Phys. Plasmas* **9** 2037
[5] Snyder P B *et al* 2011 *Nucl. Fusion* **51** 103016
[6] Burckhart A *et al* 2016 *Nucl. Fusion* **56** 056011
[7] Maggi C F *et al* 2015 *Nucl. Fusion* **55** 113031
[8] Maggi C F *et al* 2017 *Nucl. Fusion* **57** 116012
[9] Dickinson D *et al* 2014 *Phys. Plasmas* **21** 010702
[10] Bokshi A *et al* 2014 *Plasma Phys. Control. Fusion* **58** 075011
[11] Dunne M G *et al* 2017 *Plasma Phys. Control. Fusion* **59** 025010
[12] Wolfrum E *et al* 2017 *Nucl. Mater. Energy* **12** 18
[13] Harrer G F *et al* 2018 *Nucl. Fusion* **58** 112001
[14] Snyder P B *et al* 2009 *Nucl. Fusion* **49** 085035
[15] Diallo A *et al* 2014 *Phys. Rev. Lett.* **112** 115001
[16] Groebner R *et al* 2013 *Nucl. Fusion* **53** 093024
[17] Pütterich T *et al* 2011 *J. Nucl. Mater.* **415** S334–9
[18] Viezzer E *et al* 2014 *Nucl. Fusion* **54** 012003
[19] Cavedon M *et al* 2017 *Nucl. Fusion* **57** 014002
[20] Viezzer E *et al* 2017 *Nucl. Fusion* **57** 022020
[21] Kotschenreuther M *et al* 2019 *Nucl. Fusion* **59** 096001
[22] Callen J D *et al* 2010 *Nucl. Fusion* **50** 064004
[23] Told D *et al* 2008 *Phys. Plasmas* **15** 102306
[24] Peeters A *et al* 2011 *Nucl. Fusion* **51** 094027
[25] Biglari H *et al* 1990 *Phys. Fluids* B **2** 1
[26] Hatch D *et al* 2018 *Plasma Phys. Control. Fusion* **60** 084003
[27] Hinton F L and Wong S K 1985 *Phys. Fluids* **28** 10
[28] Shaing K C *et al* 1990 *Phys. Fluids* B **2** 1492
[29] Hinton F L *et al* 1999 *Phys. Lett.* A **259** 267
[30] Cavedon M *et al* 2017 *Plasma Phys. Control. Fusion* **59** 105007
[31] Viezzer E *et al* 2018 *Nucl. Fusion* **58** 026031
[32] Cavedon M *et al* 2019 *Nucl. Mater. Energy* **18** 275
[33] Groebner R *et al* 2009 *Nucl. Fusion* **49** 045013
[34] Wade M R *et al* 2005 *Phys. Rev. Lett.* **94** 225001
[35] Behn R *et al* 2007 *Plasma Phys. Control. Fusion* **49** 1289
[36] Beurskens M N A *et al* 2009 *Nucl. Fusion* **49** 125006
[37] Burckhart A *et al* 2010 *Plasma Phys. Control. Fusion* **52** 105010
[38] Scannell R *et al* 2013 *Plasma Phys. Control. Fusion* **55** 035013
[39] Diallo A *et al* 2015 *Phys. Plasmas* **22** 056111
[40] Laggner F M *et al* 2016 *Plasma Phys. Control. Fusion* **58** 065005
[41] Cavedon M *et al* 2017 *Rev. Sci. Instrum.* **88** 043103
[42] Viezzer E *et al* 2013 *Nucl. Fusion* **53** 053005
[43] Wade M R *et al* 2005 *Phys. Plasmas* **12** 056120
[44] Mink F *et al* 2018 *Nucl. Fusion* **58** 026011
[45] Laggner F M *et al* 2019 *Nucl. Mater. Energy* **19** 479
[46] Pereverzev G V *et al* 2002 *ASTRA IPP Report* **5** 98

[47] Ivanov A A *et al* 2005 *32nd EPS Conf. on Plasma Physics Tarragona* vol 29C (http://epsppd.epfl.ch/Tarragona/pdf/P5_063.pdf)

[48] Peeters A G 2000 *Phys. Plasmas* **7** 268

[49] Cavedon M *et al* 2019 *EPS Conf. on Plasma Physics, Milan* (http://ocs.ciemat.es/EPS2019PAP/pdf/P5.1069.pdf)

[50] Snyder P B *et al* 2007 *Nucl. Fusion* **47** 961

[51] Aiba N *et al* 2011 *Nucl. Fusion* **51** 073012

[52] Morales J *et al* 2016 *Phys. Plasmas* **23** 042513

[53] Burrell K H *et al* 1988 *Nucl. Fusion* **28** 3

[54] Kallenbach A *et al* 1991 *Plasma Phys. Control. Fusion* **33** 595

[55] DeGrassie J S *et al* 2003 *Nucl. Fusion* **43** 132

[56] Nishijima D *et al* 2005 *Plasma Phys. Control. Fusion* **47** 89

[57] Angioni C *et al* 2011 *Phys. Rev. Lett.* **107** 215003

[58] Solomon W M *et al* 2011 *Nucl. Fusion* **51** 073010

[59] McDermott R M *et al* 2014 *Nucl. Fusion* **54** 043009

[60] Chrystal C *et al* 2017 *Phys. Plasmas* **24** 056113

[61] Grierson B *et al* 2017 *Phys. Rev. Lett.* **118** 015002

[62] Camenen Y *et al* 2017 *Plasma Phys. Control. Fusion* **59** 034001

[63] Omotani J T *et al* 2017 *Nucl. Fusion* **57** 066048

[64] Fable E *et al* 2013 *Plasma Phys. Control. Fusion* **55** 124028

[65] Horton L D *et al* 2005 *Nucl. Fusion* **45** 856

[66] Chankin A V *et al* 2006 *Plasma Phys. Control. Fusion* **48** 839

[67] Pütterich T *et al* 2012 *Nucl. Fusion* **52** 083013

[68] Viezzer E *et al* 2013 *Plasma Phys. Control. Fusion* **55** 124037

[69] Churchill R M *et al* 2013 *Nucl. Fusion* **53** 122002

[70] Theiler C *et al* 2014 *Nucl. Fusion* **54** 083017

[71] Viezzer E *et al* 2015 *Nucl. Fusion* **55** 123002

[72] Cruz-Zabala D J *et al* 2019 *J. Instrum.* **14** C11006

[73] TRANSP User Page (https://transp.pppl.gov/index.html)

[74] Peeters A G *et al* 2007 *Phys. Rev. Lett.* **98** 265003

[75] Hatch D *et al* 2019 *Nucl. Fusion* **60** 086056